Biosensors and Bioelectronics 141 (2019) 111385

Contents lists available at ScienceDirect

Biosensors and Bioelectronics

journal homepage: www.elsevier.com/locate/bios

A self-powered photoelectrochemical biosensor for H_2O_2, and xanthine oxidase activity based on enhanced chemiluminescence resonance energy transfer through slow light effect in inverse opal TiO_2

Bekir Çakıroğlu[a], Mahmut Özacar[a,b,*]

[a] Sakarya University, Biomedical, Magnetic and Semiconductor Materials Research Center (BIMAS-RC), 54187, Sakarya, Turkey
[b] Sakarya University, Science & Arts Faculty, Department of Chemistry, 54187, Sakarya, Turkey

ARTICLE INFO

Keywords:
TiO_2 IOPCs
Photoelectrochemical sensing
CdS:Mn QDs
Xanthine oxidase
Smart materials

ABSTRACT

TiO_2 inverse opal photonic crystals (IOPCs) were fabricated by using polystyrene template. TiO_2 IOPCs based photoelectrochemical (PEC) biosensor was fabricated for the precise and stable detection of Heme without external irradiation. Then, the sensitization of TiO_2 IOPCs was fulfilled with CdS quantum dots (QDs) by SILAR method to form ITO-TiO_2 IOPCs–CdS:Mn electrode, which in turn was used to construct a PEC biosensor. The uniform porous structure of IOPCs with a large surface area is conducive to the excellent electronic transmission and QDs deposition. Also, the energy level matching between the conduction bands of CdS QDs and TiO_2 IOPCs widened the range of light absorption, allowing for electron injection from excited CdS QDs to TiO_2 upon luminol chemiluminescence, which enhanced the photocurrent. Furthermore, when the red edge of the photonic stop band of TiO_2 IOPCs overlapped with the band gap of TiO_2, and chemiluminescence emission of luminol, a substantial photocurrent increment was observed due in part to the slow light effect. The biosensor possesses a large linear detection range of 0.063–4 mM with a LOD of 19 μM for H_2O_2. Also, xanthine oxidase activity was determined with a linear measurement range of 0.01–15 mU/mL. Our strategy opens a new horizon to IOPCs based and QDs sensitized PEC sensing, which could be more sensitive, convenient and inexpensive for clinical and biological analysis. As far as we know, the largest photocurrent generation by luminol chemiluminescence was observed thanks to the use of semiconducting hybrid IOPCs material even at 0 V.

1. Introduction

The photoelectrochemical (PEC) biosensors are a hot topic in biosensor area and yield beneficial features, such as high sensitivity, low-cost production, facile operation, low background signal due to the utilization of the separate sources for excitation and detection (Zhao et al., 2017a). The PEC process refers to photon-to-current conversion within photoactive materials excited by light and includes the steps of photo-generated charge separation and transfer, oxidation-reduction reactions, and finally photocurrent generation (Çakıroğlu and Özacar, 2018). Also, PEC systems allow precise analysis at 0 V vs Ag/AgCl, which usually cannot attain by electrochemical biosensors (Akkaya et al., 2018).

Hitherto, titanium dioxide (TiO_2) has been widely used in the PEC systems as a photoactive supporter and charge collector, due to its non-toxicity, low-cost fabrication, high PEC stability, and good biocompatibility (Zhu et al., 2016). However, the excitation of TiO_2 is limited to the UV region below 430 nm, which could cause destructive effects for biomolecules, weakly visible light utilization, and high recombination rate of photo-generated charges. Overall, the low absorbance of visible light is one of the bottlenecks for the thin films of large-band gap semiconductors (Liu et al., 2017). To enhance photon collection, researchers have tended to broaden the absorption spectrum of semiconductors into visible region, and boosted the absorption efficiency via chemical routes such as element doping (Ansari et al., 2016), noble metal nanoparticles (NPs) deposition (Çakıroğlu et al., 2019), sensitization (Çakar and Özacar, 2017), p-n heterojunction formation, and physical route *viz.* increasing the path length of light by scattering and/or resonance, and accomplishment of the slow light effect in inverse opal photonic crystals (IOPCs) (Xu et al., 2015).

Currently, TiO_2 IOPCs have provided advanced photon management to enhance PEC energy conversion of semiconductors by trapping the light with multiple scattering of a certain wavelength range in the IOPCs, which intensifies the light-matter interactions without chemical

* Corresponding author. Sakarya University, Biomedical, Magnetic and Semiconductor Materials Research Center (BIMAS-RC), 54187, Sakarya, Turkey.
E-mail address: mozacar@hotmail.com (M. Özacar).

https://doi.org/10.1016/j.bios.2019.111385
Received 19 March 2019; Received in revised form 28 May 2019; Accepted 30 May 2019
Available online 03 June 2019
0956-5663/

modification for more excitation (Rinne et al., 2008; Qi et al., 2014a). IOPCs possess the advantages of photonic crystals including the slow light effect, lightweight, high surface area, and deliberately designed 3D porous architecture with easily controlled pore size (Zalfani et al., 2015; Stein et al., 2008). IOPCs possess a photonic stop band (PSB), which forbids light of certain frequencies from propagation, thus increase the effective optical path length and interaction within the material, leading to an improvement of PEC response (Zhang et al., 2014; Xia et al., 2014). IOPCs can enhance light harvesting efficiency by multiple mechanisms. Firstly, the periodic macropores structure of the TiO_2 IOPCs allows the light to penetrate deep into the film, enable multiple light reflection and scattering within the structure by leading to the increasing light absorption (Stein et al., 2008; Liao et al., 2010). Secondly, the uniform macroporous channels increase the accessible surface area, mass transportation, shorten the distance of electron diffusion and reduce the electron-hole recombination rate (Stein et al., 2008; Kwak et al., 2009). More importantly, at the red and blue edge of PSB, the group velocity of the light is significantly decreases, owing to the effect of nonlinear dispersion, creating slow light effect (Zhang et al., 2014; Qi et al., 2014b). The slow light effect can considerably increase the effective optical path length, by leading to a delay and storage of light in IOPCs (Eftekhari et al., 2017). When the energy of slow photons is in resonance with the band gap of the semiconductors with low absorbance, the photon absorption can be enhanced (Qi et al., 2014b). The diffuse distance from the surface of pore structure was shorter than the surface, which reduced the recombination of electrons (Zalfani et al., 2015). Recently, the combination of physical and chemical routes has led to the excellent PEC performance. CdS quantum dots (QDs) with a narrow band gap of ~2.4 eV is a commonly used semiconductor in PEC systems (Golub et al., 2012). However, QDs as photoactive materials usually suffer from the issues such as relatively low quantum yield, low charge separation, and photoluminescence blinking (Wang et al., 2017). The low PEC efficiency of CdS QDs has been overcome by incorporating CdS into IOPCs material by yielding unprecedented PEC response and stability, and this system can be used in PEC biosensing systems.

In this study, we aimed to enhance luminol chemiluminescence (CL) resonance energy transfer through the slow light effect in inverse opal TiO_2 based PEC biosensor for the first time. In addition, the external light intensity is linearly proportional to the analyte concentration, which leads to even more enhancement in the sensitivity of PEC biosensing system compared to ordinary PEC biosensors. To this end, we designed a novel ITO-TiO_2 IOPCs–CdS: Mn electrode to maximize photon absorbance at the electronic absorption edge, and CL triggered PEC biosensing system was fabricated for H_2O_2 and xanthine oxidase activity detection at 0 V *viz.* on self-powered mode without intricate procedures. The photocurrent of modified electrode was found to be 22 times larger than that of thin film modified electrode, due to the slow light effect and multiple scattering of IOPCs structure.

2. Materials and methods

2.1. Preparation of polystyrene colloidal crystal template arrays

The ITO electrodes (75 mm length × 25 mm width × 1.1 mm thickness; surface resistivity 8–12 Ω/sq) were sequentially pre-cleaned by sonication in acetone, sodium hydroxide solution (1 M), in ethanol/water mixture (1:1, v/v), and water for 15 min, before being dried in a vacuum oven. Next, polystyrene (PS) colloidal crystal template arrays were self-assembled using the vertical deposition process. In a 10 mL beaker, 5 mL of PS suspension was ultrasonically dispersed, and an ITO substrate was vertically placed in the PS suspension. The beaker was placed in an oven at 70 °C for 24 h for the evaporation of the solvent to achieve a self-assembled face-centered cubic PS opal template on the ITO.

2.2. Preparation of TiO_2 inverse opal photonic crystals

Subsequently, the TiO_2 inverse opal structure was obtained through dip-coating and calcination. The sol-gel precursor solution was prepared as follows. 5.6 mL TIP, 45 mL ethanol and 1 mL acetylacetone were mixed and stirred, after which 0.85 mL hydrochloric acid and 4.6 mL deionized water (DW) were added into the mixture, and stirred for 1 h. Next, PS templates were dipped into the as-prepared precursor solution once for the infiltration of precursor solution into the voids in the opal template by capillary force. The dip-coated electrodes were kept in the oven at 75 °C for 24 h, and then calcined at 450 °C for 30 min (heating rate was 1 °C/min) to remove the PS template, and obtain anatase form. The obtained electrode is designated as ITO-TiO_2 IOPCs. Also, the same amount TiO_2 precursor was used to form ITO-TiO_2 thin film electrode for the comparison of the performances.

CdS:Mn was deposited on the electrode surface by successive ionic layer adsorption and reaction (SILAR) technique. The TiO_2 IOPCs coated ITO electrodes were dipped into 0.1 M cadmium acetate mixed with 0.08 M manganese(II) acetate in methanol for 2 min, rinsed with ethanol and then immersed into 0.1 M sodium sulfide in DW for 2 min, again rinsed with ethanol. This cycle was repeated up to 14 times. The products were dried at 60 °C in an oven.

3. Results and discussion

3.1. Properties of IOPCs

Fabrication of the ITO-TiO_2 IOPCs–CdS:Mn electrode was illustrated in Scheme 1A. The resulting products displayed strong opalescence under incident light. The top-view TEM image of the TiO_2 IOPCs structure showed face-centered-cubic (fcc) ordering of air spheres in a long-range well-ordered hexagonal arrangement over the entire sample with a close-packed plane (111) oriented parallel to the substrate (Fig. 1A, B, C). The center-to-center distance of IOPCs was found to be 185 nm, which is about 30% smaller than the original size of the PS sphere due to the shrinkage of spheres' diameters during calcination. The CdS:Mn precursor solution can easily penetrate into the TiO_2 IOPCs owing to its high porosity. As a result, a uniformly deposited CdS:Mn NPs could be observed on the surface of IOPCs (Fig. 1D). The pore size is further reduced to 160 nm, and the thickness of the deposited CdS:Mn NPs was estimated to be ca. 7.5 nm. Fig. 1E shows the high-resolution TEM (HRTEM) image of the CdS:Mn QDs on IOPCs, and two different fringe spacings were determined to be ~0.36 nm and ~0.25 nm, which correspond to (101) lattice plane of anatase TiO_2 and (102) lattice plane of QDs, respectively. The energy dispersive X-ray spectrum of ITO-TiO_2 IOPCs–CdS:Mn evidently confirms the existence of Ti, O, Cd, Mn and S elements (Fig. S1). Strong peaks for Ti and O indicate the abundance of TiO_2. To further determine the specific distribution of Ti, O, Cd, S and Mn elements, EDX mappings of ITO-TiO_2 IOPCs– CdS:Mn were taken (Fig. 1F). It can be clearly seen that the distribution of Ti and O elements is homogeneous and the corresponding location of O matches well with that of Ti. Moreover, the distribution of Cd, S, and Mn mainly disperses on the surface of IOPCs.

Owing to the fact that the structure of IOPCs could increase absorption of incident light of certain wavelength, we investigated how the change of PSB influenced on the absorption of incident light. Theoretically, the normal positions of the PSBs in fcc opal and inverse opal PCs can be tuned by varying the size of PS spheres, and estimated by Bragg's law of diffraction combined with Snell's law as the following equation (Xia et al., 2014):

$$\lambda = 2\sqrt{\frac{2}{3}}\, D\sqrt{n_{eff}^2 - \sin^2\theta} \quad (1)$$

$$n_{eff} = n_{solid}\varphi + n_{medium}(1 - \varphi) \quad (2)$$

λ is the wavelength of the photonic stop band, D is the pore size of the

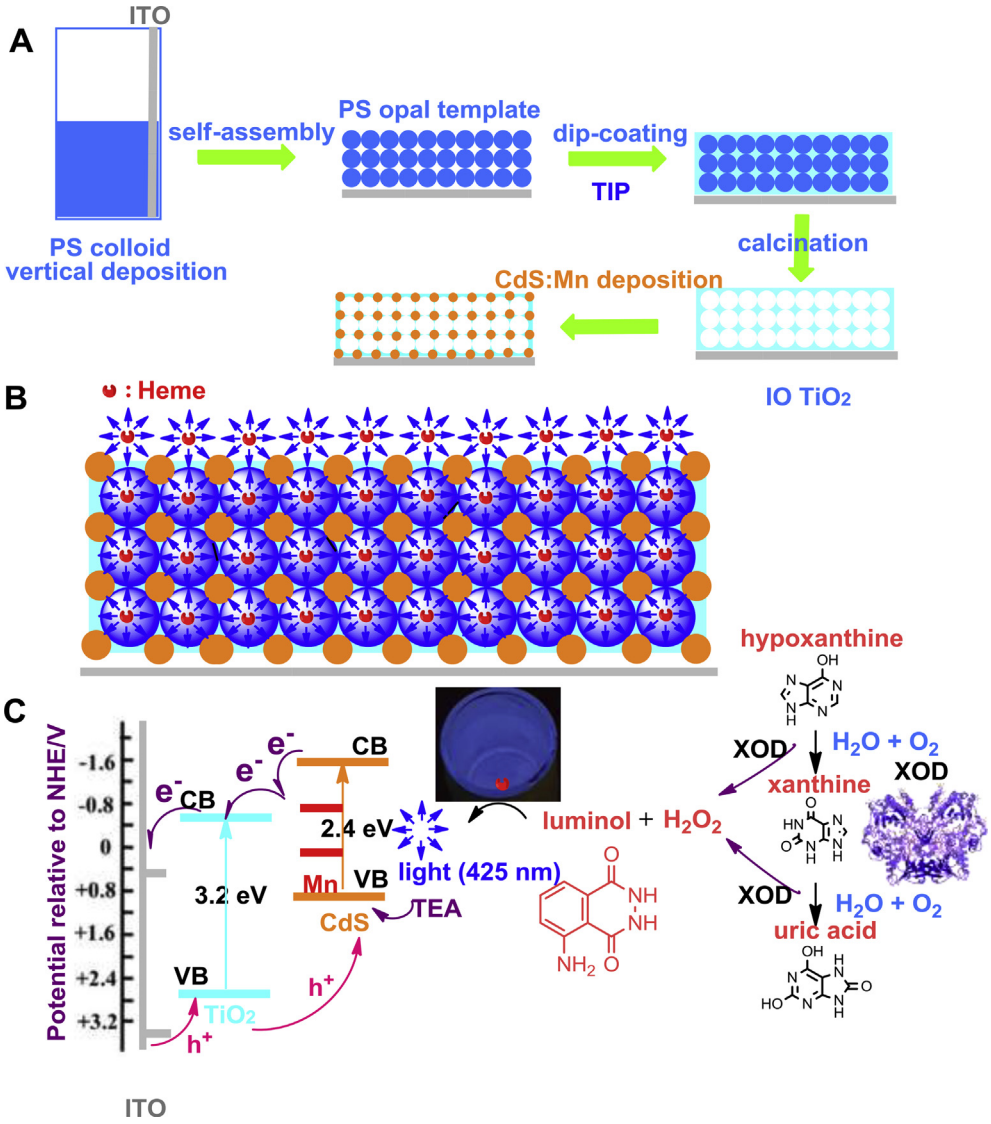

Scheme 1. A. Illustration of the fabrication process of ITO-TiO_2 IOPCs– CdS:Mn electrode, B. Multiple CL scattering inside IOPCs, C. Photo-generated electron transfer through the PEC biosensor.

IOPCs, θ is the angle of incident light, which is 0° in this study, n_{eff} is the effective refractive index of IOPCs, n_{solid} and n_{medium} are the refractive index of TiO_2 (2.54) and the medium within the pores, *viz.* Tris-HCl buffer (1.35), and air (1.00) respectively. φ is the IOPCs phase volume percentage, which corresponds to 0.26 for a closed-packed inverse opal structure. Fig. 2A shows the reflection spectra of thin film and IOPCs while varying the microsphere diameters. The reflection peaks represent the PSB of the structures. The stop bands wavelengths increased with enlarging diameter of PS spheres. Also, in Fig. 2B, the location of the PSBs displays a linear relationship with the pore size of IOPCs.

UV–Vis light absorption spectra have further confirmed the location of the stop bands of TiO_2 IOPCs in Tris-HCl buffer (Fig. 2C). An increment of light absorption in red and blue edge of PSB was observed for each TiO_2 IOPCs, and the enhancement shifts progressively to longer wavelengths with increasing pore diameter. The data of the PSBs were listed in Table S2. Herein, the calculated PSB were calculated according to Eq. (1) and the measured PSBs were estimated from Fig. 2A, and C. The difference between the calculated and measured PSB values originates from the incomplete infiltration of TiO_2 precursor, which makes φ in Eq. (1) smaller than 0.26, and the shrinkage of spheres' diameters during calcinations (Qi et al., 2014b). Nevertheless, enhanced absorption regions are at the edge of photonic stop bands results from the slow light effect, which implies that light has its highest amplitude in the high refractive index part of IOPCs. Herein, light waves are localized in different parts of the structure, depending on their energy, and thus IOPCs interact more strongly with the red edge photons of the PSB compared to the blue edge photons (Liao et al., 2010). Therefore, light absorption of the IOPCS modified electrodes can be stronger by adjusting the band gap to red side of the PSB. It must be kept in mind that when the absorption peak overlaps the PSB, the group velocity of light is faster than that at the edge of the PSB, and light-matter interaction decreases. According to Rayleigh scattering, the intensity of scattering is inversely proportional with the fourth power of the wavelength. Hence, photons in the blue spectral region should be more efficiently backscattered by the defects in the IOPCs (Wang et al., 2008).

In Fig. 2D, upon CdS:Mn sensitization, enhanced light absorption occurs near the blue and red edge of a PSB centered at 490 nm, and the absorption spectrum blue shifted due to the diminishment in the diameter of IOPCs by covering the high energy wavelength range of CL. The gain in light harvesting is attributed to the trapping light in IOPCs, and slow light effect combining with the great CL absorbance of CdS:Mn QDs. Also, in Fig. 2D, the absorption spectrum of intact electrode overlaps with the CL spectrum of luminol (λ_{max} = 438 nm), and substantial light absorption at the red and blue edge of the PBG was

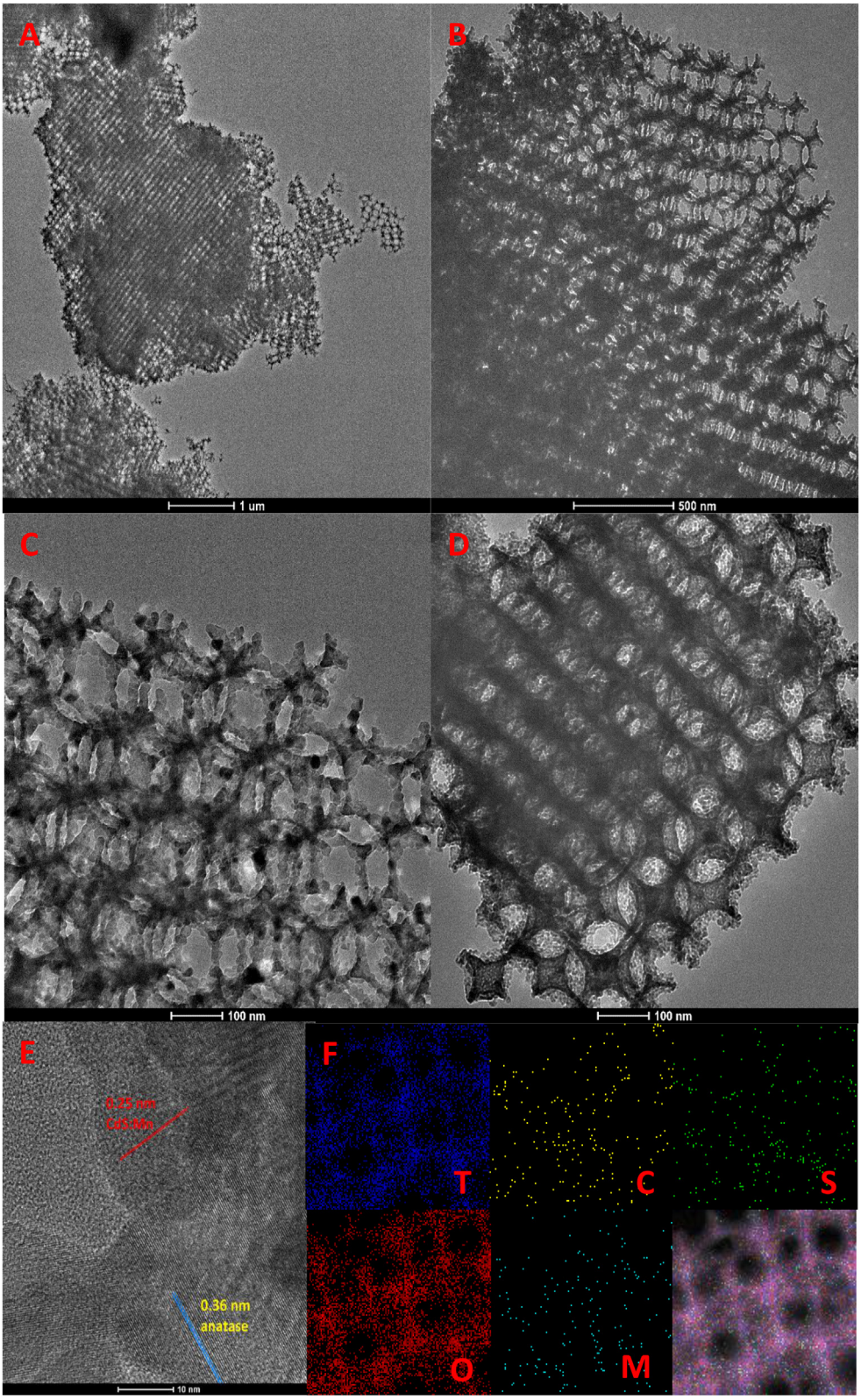

Fig. 1. The top-view TEM images of A, B, C. ITO-TiO_2 IOPCs, and D. ITO-TiO_2 IOPCs– CdS:Mn, E. HRTEM image of ITO-TiO_2 IOPCs– CdS:Mn, F. Elemental mapping images of ITO-TiO_2 IOPCs– CdS:Mn.

observed.

Fig. 3A shows the photocurrent spectra of electrodes under monochromatic illumination as a function of the wavelength of the incident light. ITO-TiO_2 IOPCs electrodes shows a significant response nearly in the CL region of luminol. Herein, IOPCs can enhance light harvesting efficiency by multiple mechanisms. Firstly, the open macroporous structure of the TiO_2 IOPCs allows the light to penetrate deep into the film, circulate inside semiconductor IOPCs. Also, the periodic structure and the interconnected network can enhance light absorption, and shorten the distance of electron diffusion, and facilitate the capability of

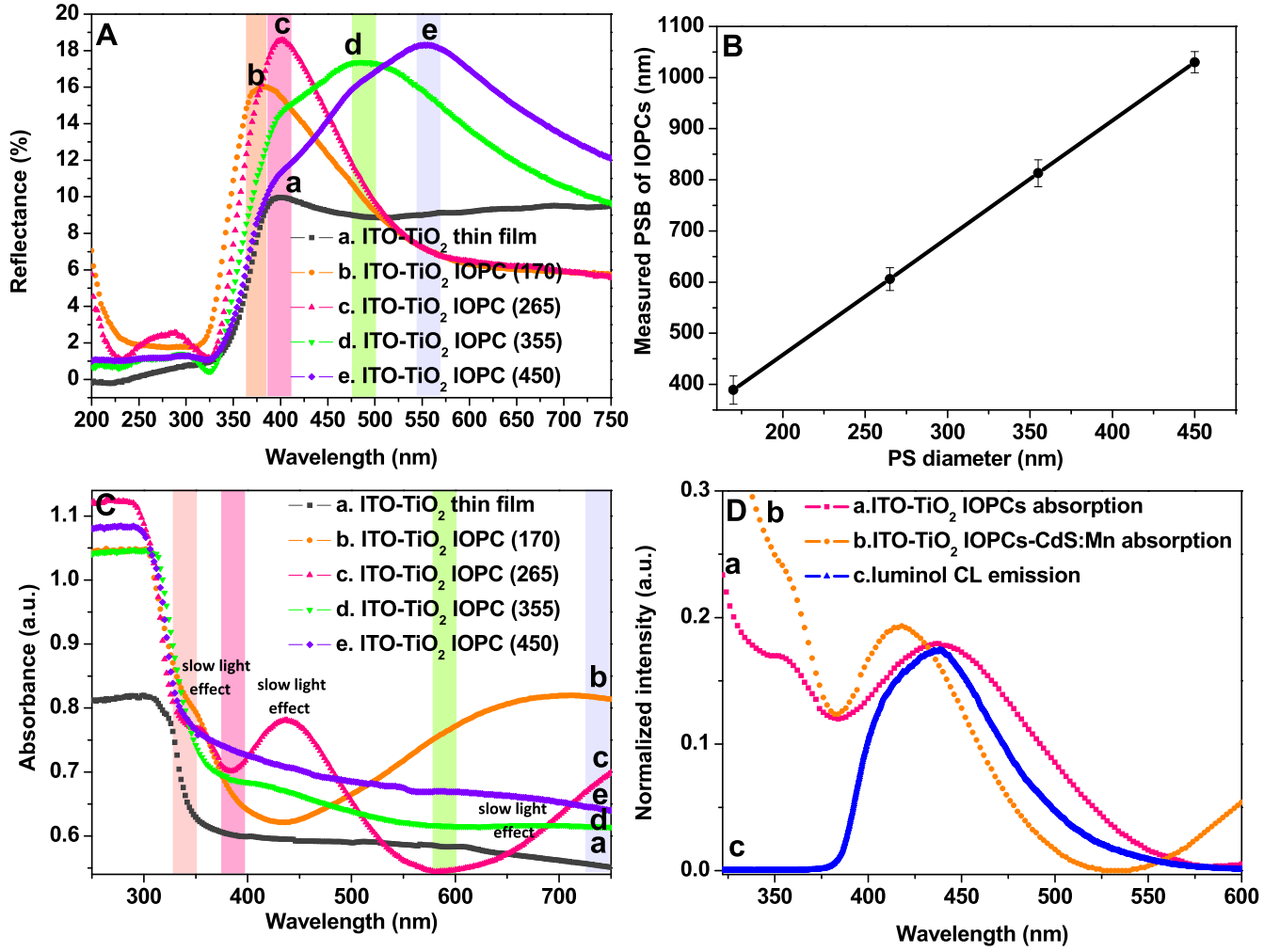

Fig. 2. A. Reflectance spectra of ITO-TiO_2 thin film, and ITO-TiO_2 IOPCs (Spectra were recorded in air and at the normal (θ = 0°) direction), B. Dependence of PSB positions on PS sphere diameter, C. UV–visible absorbance spectra of ITO-TiO_2 thin film, and ITO-TiO_2 IOPCs (Spectra were recorded in Tris-HCl buffer and at the normal (θ = 0°) direction), D. Luminol emission spectrum, and absorbance spectrum of electrodes.

electron transfer (Zalfani et al., 2015; Kwak et al., 2009). The light near its frequency edges of PSB undergoes multiple scattering and travel with strongly reduced group velocity, which gives rise to the slow photon effect enabling enhanced light-matter interaction, and improved light absorption without chemical modification (Zalfani et al., 2015). Also, at the red edge of the PSB, the incident light is localized on the dielectric material *viz*. TiO_2. The red edge of the PSB of ITO-TiO_2 IOPCs–CdS:Mn was tuned by overlapping with the electronic absorption band edge of the electrode (3.08 eV; 410 nm), which lies in the CL emission of luminol, and this, in turn, gives rise to an increased generation of electron-hole pairs and higher photocurrent generation due in part to the longer photon lifetime in the IOPCs, high CL absorption of QDs. All of the above indicates that CL could be effectively utilized for PEC sensors, in which the transportation and separation of photoexcited charge carriers are efficient in the material.

The optical band gaps of the obtained PEC systems were calculated according to the Tauc formula below (Çakıroğlu and Özacar, 2018):

$$\alpha = A.\ (h\nu\ -\ E_g)^n/h\nu \quad (3)$$

A is a constant, α is the absorption coefficient, hν is the energy of electromagnetic irradiation, E_g is the optical band gap of the materials and the exponent n depends on the type of transition and have values 1/2, 2, 3/2 and 3 corresponding to the allowed direct, allowed indirect, forbidden direct and forbidden indirect transitions, respectively. Herein, n corresponds to 2 for both materials (indirect transition). The optical band gap values were calculated by extrapolating the straight line portion of $(\alpha h\nu)^{1/n}$ versus hν as shown in Fig. 3B, and the band gaps were found to be E_g = 3.18 eV (390 nm) for ITO-TiO_2 IOPCs, and E_g = 3.05 eV (407 nm) for ITO-TiO_2 IOPCs–CdS:Mn, respectively. Thus, CdS:Mn NPs reduced the intact electrode band gap to the wavelength, which is more beneficial for the absorption of luminol CL in the PEC biosensing system.

According to the linear sweep voltammetry (LSV) measurements, the potential value became constant at 0 V, which is beneficial for self-powered operation (Fig. 3C). Also, the increasing potential displayed rapid, and substantial current change, probably owing to the oxidation of the composite, and negative potential from −0.1 V can inhibit the electron transfer from the electrode composite to the electrode by leading to high electron-hole recombination. Thus, 0 V was chosen as operation potential to construct self-powered biosensor.

3.2. PEC electron transfer through ITO-TiO_2 IOPCs–CdS:Mn electrode

To clearly understand the PEC sensing process, a schematic illustration of the principles of luminol CL triggered PEC determination of H_2O_2, and xanthine oxidase activity based on light intensity was illustrated in Scheme 1B. The putative type II (staggered) junction formation was demonstrated in Scheme 1C. Upon chemiluminescent illumination, the simultaneous excitation of TiO_2 IOPCs and CdS:Mn NPs leads to the formation of electron-hole pairs in each of the

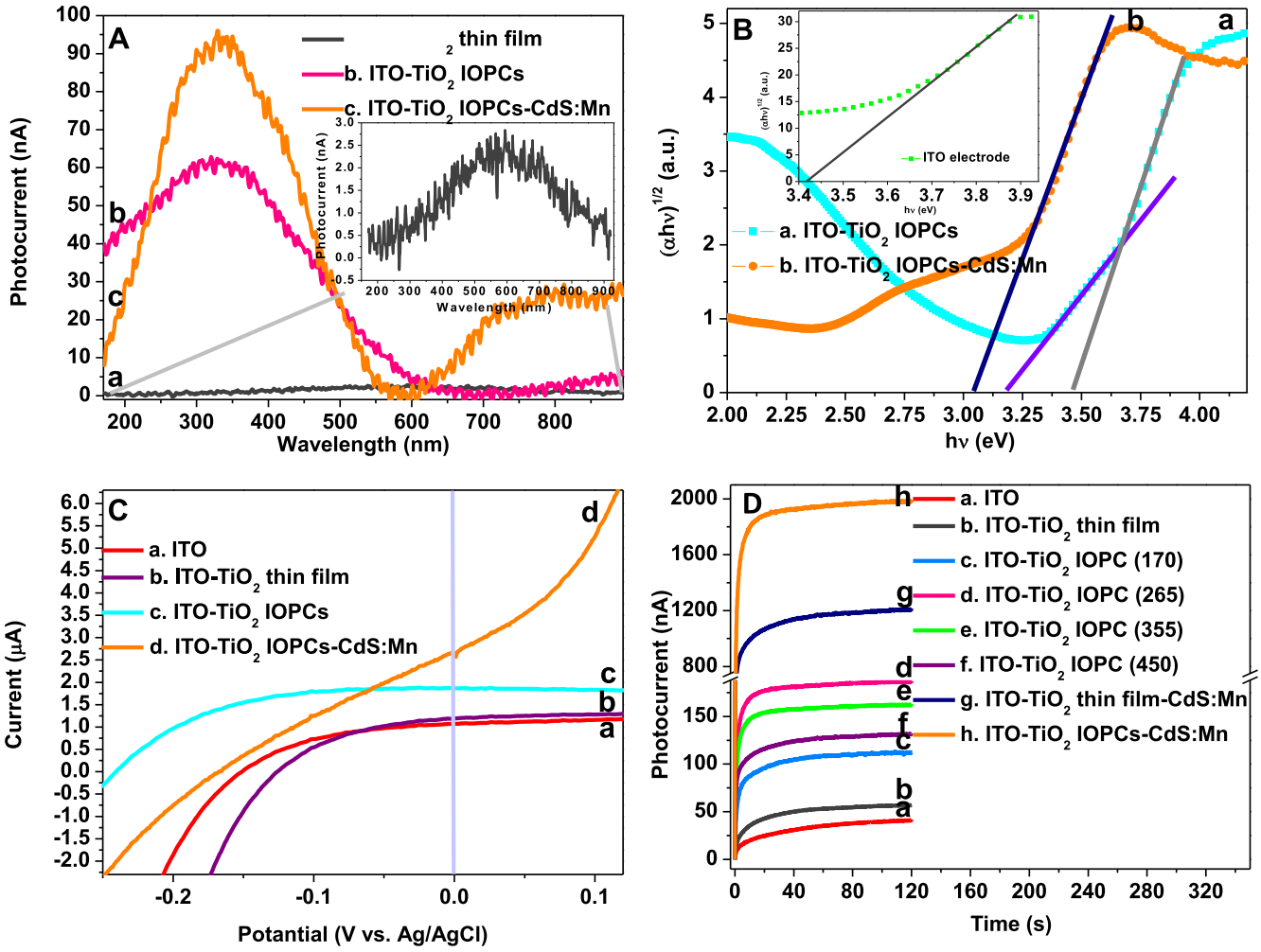

Fig. 3. A. Photocurrent-wavelength curve of a. ITO-TiO_2 thin film, b. ITO-TiO_2 IOPCs, and c. ITO-TiO_2 IOPCs– CdS:Mn, B. Kubelka-Munk function versus energy of light plots of a. ITO-TiO_2 IOPCs, b. ITO-TiO_2 IOPCs– CdS:Mn (inset: pristine ITO), C. The potential vs. photocurrent generation curves, D. Time-dependent photocurrent generation of a. ITO, b. TiO_2 thin film, c. ITO-TiO_2 IOPCs (170), d. ITO-TiO_2 IOPCs (265), e. ITO-TiO_2 IOPCs (355), f. ITO-TiO_2 IOPCs (450), g. ITO-TiO_2 thin film– CdS:Mn h. ITO-TiO_2 IOPCs– CdS:Mn under luminol CL at 0 V.

semiconductors. As shown in Scheme 1C, the conduction and valence band edges are −3.9 eV and −7.6 eV for TiO_2 and -3.5 eV and −5.6 eV for QDs. The conduction band edge of QDs is higher than that of TiO_2. Therefore, the effective matching of the conduction bands of semiconductors leads to the easy transportation of the photogenerated electrons from the conduction band of CdS:Mn QDs to ITO electrode through TiO_2 IOPCs. This process effectively suppresses the charge recombination of QDs and extends their light-capturing ability by leading to an improvement in the photocurrent generation. Also, the large valence band energy barrier between the CdS:Mn QDs and TiO_2 IOPCs facilitates the transportation of photogenerated holes from the valence band of TiO_2 IOPCs to that of CdS:Mn. Consequently, CdS:Mn QDs sensitized TiO_2 IOPCs enhances the absorption of luminol CL, along with the improvement of the separation of photo-generated charges. TEA was used as an electron donor to scavenge the photogenerated holes in CdS:Mn QDs.

3.3. Photocurrent generation by ITO-TiO_2 IOPCs–CdS:Mn electrode and H_2O_2 and XOD activity measurements

Fig. 3D displays the photocurrent generations of the different photoelectrodes in TEA containing 0.1 M Tris-HCl buffer (pH 9.0). The bare ITO electrode generated a small photocurrent response under luminol CL. The TiO_2 thin film coated electrode increased the photocurrent to some extent. Although TiO_2 is excited with UV radiation, it can also undergo excitation under CL emission (Tan et al., 2016). The photocurrents of the TiO_2 IOPCs were superior to the TiO_2 thin film prepared by the similar way without using the PS sphere. This finding can be attributed to the excellent features of IOPCs, such as slow light effect and multiple scattering of inverse opal structure (Zhang et al., 2014; Boppella et al., 2017). Also, high specific surface area leads to the improvement of luminol CL absorption. Especially, the PSB of ITO-TiO_2 IOPCs prepared with PS spheres with 265 nm diameter is in the vicinity of 390 nm, which is near the band absorption of TiO_2 (3.18 eV). Therefore, this electrode exhibited the highest photocurrent generation among all four IOPCs due to the blue edge of PSB overlapped well with the band absorption of TiO_2, and some part of the luminol CL emission includes this wavelength range. In IOPCs, the wavelengths below the PSB could only cause to the strong light scattering, which enhance photocurrent (Collins et al., 2016). Therefore, ITO-TiO_2 IOPCs electrodes prepared with PS spheres with 355, and 450 nm diameter showed the high photocurrent after ITO-TiO_2 IOPCs (265). ITO-TiO_2 IOPC (265) electrode was sensitized with Mn-doped CdS QDs, and the photocurrent substantially increased by an order of magnitude owing to the fact that the band gap of the electrode shifted to the blue edge of the PSB of ITO-TiO_2 IOPC (265)-CdS:Mn and most part of the luminol CL emission includes this wavelength range by leading to the slow light effect in inverse opal structure. Thus, significant enhancement of light

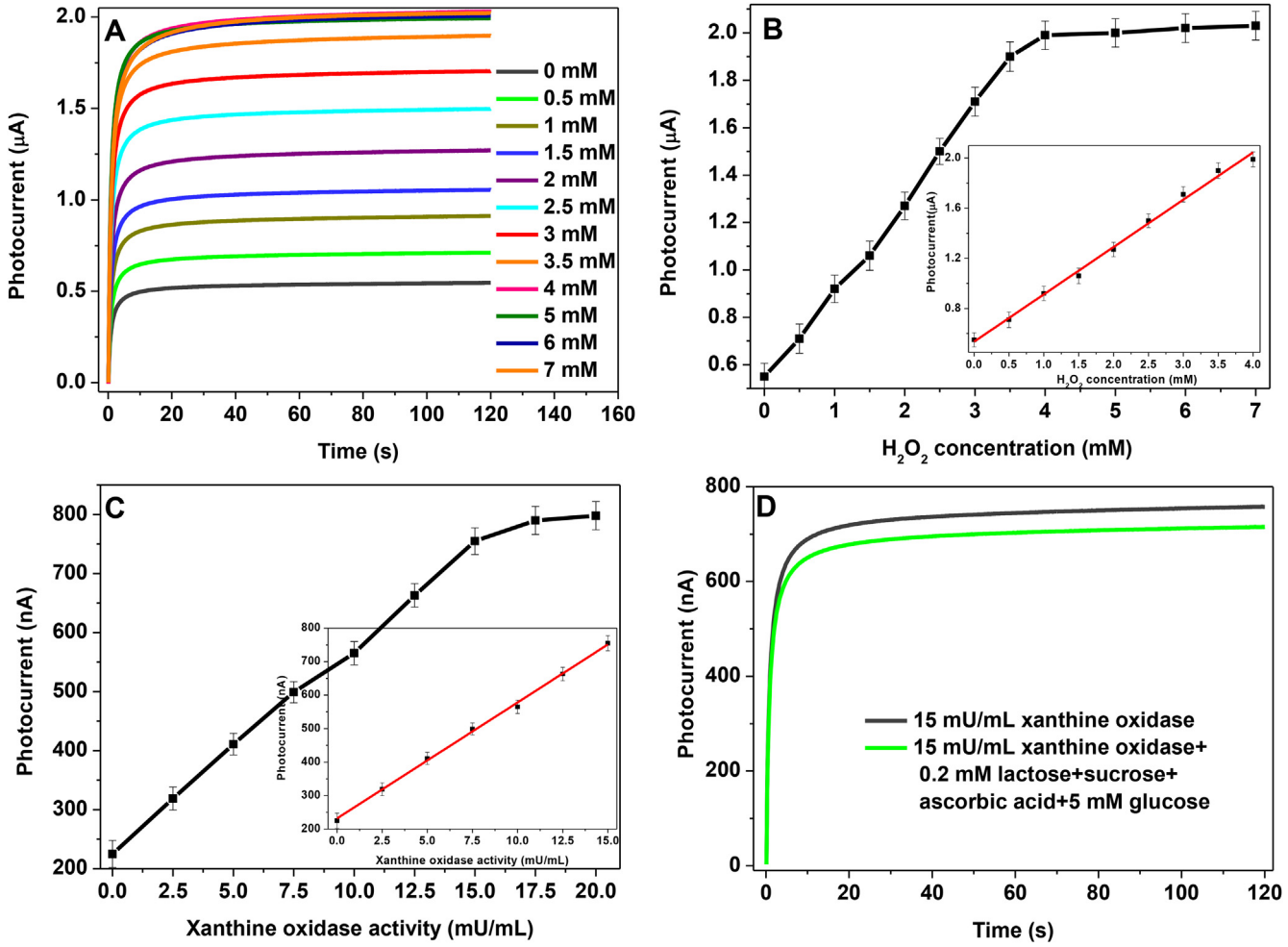

Fig. 4. A. Photocurrent response of ITO-TiO_2 IOPCs– CdS:Mn electrode with different concentrations of H_2O_2 under luminol CL at 0 V, B. The photocurrent vs. concentration graph (inset: the linear part of the graph, Error bars indicate the standard deviation of repeated 3 measurements), C. The photocurrent vs. xanthine oxidase activity graph (inset: the linear part of the graph), D. The interfering effect on xanthine oxidase activity.

harvesting induced by the slow light effect increased the photocurrent generation. According to Fig. 2D, the absorption in high energy wavelength of CL emission also increased, which resulted in increased photocurrent generation. The porous structure of IOPCs provide long-range ordered paths for electron transport throughout the interconnected periodic structure, which results in improved charge migration (Kwak et al., 2009). Also, IOPCs facilitated Heme, and substrate movement in a highly ordered channel coupled with an enhanced photon scattering, and absorption by the slow photon effect.

The photocurrent measurements were taken in TEA solution in 0.1 Tris-HCl buffer (pH 9.0). The water reduction by photo-generated electrons was realized on the Pt electrode by producing H_2. Fig. 4A presents the photocurrent vs. time curves of ITO-TiO_2 IOPC-CdS:Mn electrodes at different H_2O_2 concentrations. The photocurrents were linearly increased up to 4 mM, then reached a plateau (Fig. 3B), which comply with the Michaelis-Menten kinetics (Çakıroğlu and Özacar, 2017). According to the linear part of the graph, the equation was found to be I (μA) = 0.3477.C (mM) + 0.56 (R^2 = 0.9951) (Fig. 3B inset) with the sensitivity of 0.35 $\mu A mM^{-1} cm^{-2}$. The limit of detection (LOD) based on 3x(standard deviation of 10 blank measurements/sensitivity) was calculated as 19 μM. The limit of quantification based on 10x (standard deviation of 10 blank measurements/sensitivity) was estimated to be 63 μM. The performance comparison was given in Table 1. When compared to the literature, a large measurement range for H_2O_2 was observed at 0 V operation voltage, which is of great importance in self-powered biosensor systems. This finding comes from the linear catalysis rate by Heme at large H_2O_2 concentration range (Zhang and Oyama, 2004). The reported studies utilized the intense incident lights, thus larger sensitivity values were observed compared to the current study.

Nowadays, XOD activity determination is of great importance, and serves as a sensitive indicator of various liver disorders. XOD can oxidase the hypoxanthine to xanthine, and then uric acid by releasing hydrogen peroxide in each step. Therefore, a large amount of H_2O_2 can induce the CL. By using PEC biosensor, the XOD activity was measured in Tris-HCl buffer (0.1 M, pH 8.0). Herein, XOD exhibited the optimum enzyme activity at pH 8.0 and this pH was chosen for the XOD activity detection. According to Fig. 4C, photocurrent increased linearly in the XOD activity range of 0.01–15 mU/mL. Therefore, XOD activity was determined in a low-cost, and self-powered mode for the first time.

4. Conclusions

In summary, we have designed a novel ITO-TiO_2 IOPCs–CdS:Mn electrode to maximize photon absorbance at the electronic absorption edge, and its luminol CL triggered PEC biosensing properties were carefully studied for H_2O_2, and xanthine oxidase activity detection. The photocurrent of modified electrode was 22 times larger than that of thin film modified electrode, due to the slow light effect and multiple scattering of IOPCs structure. In addition, the employment of external light leads to even more improvement in the sensitivity of PEC biosensing system compared to ordinary PEC biosensors by substantially

Table 1
Comparison of the performance of PEC H_2O_2 biosensors.

Biosensor material	Potential (V vs. Ag/AgCl)	LOD (μM)	Linear range (mM)	Sensitivity/($\mu A mM^{-1} cm^{-2}$)	Ref.
ITO-TiO_2 IOPCs– CdS:Mn	0	19	0.063–4	0.35	Herein
ITO-NiO-hemin	−0.05	0.1	0.0005–0.5	–	Gu et al. (2015)
Au-SAM-Au NCs[a]	−0.5	35	0–3	4.33 $nAmM^{-1}$	Zhang et al. (2015)
FTO-WO_3-CdS QDs	0	0.0027	5.10^{-6}-0.1	–	Wang et al. (2016)
TiC/C-WO_3[b]	0.64	0.003	0.01–0.5	386	Zhang et al. (2013)
FTO-ITO-CuO	0.1	180	0.1–1.0	46.4	Rehosek et al. (2016)
TiO_2 NW-Ag QDs	0.15	1200	0–22.5	8.33	Yu et al. (2015)
FTO-ZnO-ZIF-8 NRs[c]	0.54	–	0–0.4	–	Zhan et al. (2013)
Au-GO-Au NCs	−0.5	2	0.03–5	25.76 $nAmM^{-1}$	Zhao et al. (2017b)
ITO-Cu_2O–TiO_2	−0.2	0.15	0.330–16.6	181.1	Li et al. (2015)

[a] Gold nanoclusters.
[b] Carbon-doped titanium carbide.
[c] ZnO-ZIF-8 Nanorods.

reducing background noises. The porous structure of IOPCs with a large surface area led to the excellent electron transmission, and QDs deposition. PEC biosensor also showed acceptable reproducibility, and excellent selectivity, and anti-interference property. By using green chemistry and PEC systems with high photon-to-current efficiency values, futuristic IOPCs based PEC biosensors and biofuel cells can be designed in the nanobiotechnology area.

CRediT authorship contribution statement

Bekir Çakıroğlu: Methodology, Data curation, Writing - original draft, Software. **Mahmut Özacar:** Writing - review & editing, Supervision.

Acknowledgments

M.O. thanks Turkish Academy of Sciences (TUBA) for the partial support.

Appendix A. Supplementary data

Supplementary data to this article can be found online at https://doi.org/10.1016/j.bios.2019.111385.

Declaration of interests

The authors declare that they have no known competing financial interests or personal relationships that could have appeared to influence the work reported in this paper.

References

Akkaya, B., Çakıroğlu, B., Özacar, M., 2018. ACS Sustain. Chem. Eng. 6 (3), 3805–3814.
Ansari, S.A., Khan, M.M., Ansari, M.O., Cho, M.H., 2016. New J. Chem. 40 (4), 3000–3009.
Boppella, R., Kochuveedu, S.T., Kim, H., Jeong, M.J., Marques Mota, F., Park, J.H., Kim, D.H., 2017. ACS Appl. Mater. Interfaces 9 (8), 7075–7083.
Collins, G., Armstrong, E., McNulty, D., O'Hanlon, S., Geaney, H., O'Dwyer, C., 2016. Sci. Technol. Adv. Mater. 17 (1), 563–582.
Çakar, S., Özacar, M., 2017. J. Photochem. Photobiol. A Chem. 346, 512–522.
Çakıroğlu, B., Özacar, M., 2017. Electroanalysis 29, 2719–2726.
Çakıroğlu, B., Özacar, M., 2018. Biosens. Bioelectron. 119, 34–41.
Çakıroğlu, B., Demirci, Y.C., Gökgöz, E., Özacar, M., 2019. Sensor. Actuator. B Chem. 282, 282–289.
Eftekhari, E., Broisson, P., Aravindakshan, N., Wu, Z., Cole, I.S., Li, X., Zhao, D., Li, Q., 2017. J. Mater. Chem. 5 (25), 12803–12810.
Golub, E., Niazov, A., Freeman, R., Zatsepin, M., Willner, I., 2012. J. Phys. Chem. C 116, 13827–13834.
Gu, T.T., Wu, X.M., Dong, Y.M., Wang, G.L., 2015. J. Electroanal. Chem. 759, 27–31.
Kwak, E.S., Lee, W., Park, N.C., Kim, J., Lee, H., 2009. Adv. Funct. Mater. 19 (7), 1093–1099.
Li, Z., Xin, Y., Zhang, Z., 2015. Anal. Chem. 87 (20), 10491–10497.
Liao, G. aozu, Chen, S., Quan, X., Chen, H., Zhang, Y., 2010. Environ. Sci. Technol. 44, 3481–3485.
Liu, X., Huo, X., Liu, P., Tang, Y., Xu, J., Liu, X., Zhou, Y., 2017. Electrochim. Acta 242, 327–336.
Qi, D., Lu, L., Wang, L., Zhang, J., 2014a. J. Am. Chem. Soc. 136 (28), 9886–9889.
Qi, D., Lu, L., Xi, Z., Wang, L., Zhang, J., 2014b. Appl. Catal. B Environ. 160–161 (1), 621–628.
Rehosek, M., Mitoraj, D., Bledowski, M., Beranek, R., 2016. Electroanalysis 28 (10), 2327–2334.
Rinne, S.A., García-Santamaría, F., Braun, P.V., 2008. Nat. Photon. 2 (1), 52–56.
Stein, A., Li, F., Denny, N.R., 2008. Chem. Mater. 20 (3), 649–666.
Tan, F., Li, T., Wang, N., Lai, S.K., Tsoi, C.C., Yu, W., Zhang, X., 2016. Sci. Rep. 6, 1–10.
Wang, H., Zhang, Q., Yin, H., Wang, M., Jiang, W., Ai, S., 2017. Biosens. Bioelectron. 95 (January), 124–130.
Wang, W., Yang, X., Cui, H., 2008. J. Phys. Chem. C 112 (42), 16348–16353.
Wang, Y., Gao, C., Ge, S., Yu, J., Yan, M., 2016. Biosens. Bioelectron. 85, 205–211.
Xia, L., Song, J., Xu, R., Liu, D., Dong, B., Xu, L., Song, H., 2014. Biosens. Bioelectron. 59, 350–357.
Xu, R., Jiang, Y., Xia, L., Zhang, T., Xu, L., Zhang, S., Liu, D., Song, H., 2015. Biosens. Bioelectron. 74, 411–417.
Yu, L., Zhang, Y., Zhi, Q., Wang, Q., Gittleson, F.S., Li, J., Taylor, A.D., 2015. Sensor. Actuator. B Chem. 211, 111–115.
Zalfani, M., Van Der Schueren, B., Hu, Z.Y., Rooke, J.C., Bourguiga, R., Wu, M., Li, Y., Van Tendeloo, G., Su, B.L., 2015. J. Mater. Chem. 3 (42), 21244–21256.
Zhan, W.W., Kuang, Q., Zhou, J.Z., Kong, X.J., Xie, Z.X., Zheng, L.S., 2013. J. Am. Chem. Soc. 135 (5), 1926–1933.
Zhang, J., Oyama, M., 2004. Electrochim. Acta 50, 85–90.
Zhang, J., Tu, L., Zhao, S., Liu, G., Wang, Y., Wang, Y., Yue, Z., 2015. Biosens. Bioelectron. 67, 296–302.
Zhang, X., Li, L., Peng, X., Chen, R., Huo, K., Chu, P.K., 2013. Electrochim. Acta 108, 491–496.
Zhang, X., Liu, Y., Lee, S.T., Yang, S., Kang, Z., 2014. Energy Environ. Sci. 7 (4), 1409–1419.
Zhao, W.-W., Xu, J.-J., Chen, H.-Y., 2017a. Biosens. Bioelectron. 92, 294–304.
Zhao, S., Zhang, J., Li, Z., Zhang, P., Li, Y., Liu, G., Wang, Y., Yue, Z., 2017b. Microchim. Acta 184 (3), 677–686.
Zhu, J., Huo, X., Liu, X., Ju, H., 2016. ACS Appl. Mater. Interfaces 8 (1), 341–349.